

THE POWER SPECTRUM OF THE MILKY WAY: VELOCITY FLUCTUATIONS IN THE GALACTIC DISK

JO BOVY^{1,2,3}, JONATHAN C. BIRD^{4,5}, ANA E. GARCÍA PÉREZ^{6,7}, STEVEN R. MAJEWSKI⁶, DAVID L. NIDEVER⁸, AND GAIL ZASOWSKI⁹

ABSTRACT

We investigate the kinematics of stars in the mid-plane of the Milky Way on scales between 25 pc and 10 kpc with data from the Apache Point Observatory Galactic Evolution Experiment (APOGEE), the Radial Velocity Experiment (RAVE), and the Geneva-Copenhagen Survey (GCS). Using red-clump stars in APOGEE, we determine the large-scale line-of-sight velocity field out to 5 kpc from the Sun in $(0.75 \text{ kpc})^2$ bins. The solar motion $V_{\odot-c}$ with respect to the circular velocity V_c is the largest contribution to the power on large scales after subtracting an axisymmetric rotation field; we determine the solar motion by minimizing the large-scale power to be $V_{\odot-c} = 24 \pm 1$ (ran.) ± 2 (syst. $[V_c]$) ± 5 (syst. [large-scale]) km s^{-1} , where the systematic uncertainty is due to (a) a conservative 20 km s^{-1} uncertainty in V_c and (b) the estimated power on unobserved larger scales. Combining the APOGEE peculiar-velocity field with red-clump stars in RAVE out to 2 kpc from the Sun and with local GCS stars, we determine the power spectrum of residual velocity fluctuations in the Milky Way's disk on scales between $0.2 \text{ kpc}^{-1} \leq k \leq 40 \text{ kpc}^{-1}$. Most of the power is contained in a broad peak between $0.2 \text{ kpc}^{-1} < k < 0.9 \text{ kpc}^{-1}$. We investigate the expected power spectrum for various non-axisymmetric perturbations and demonstrate that the central bar with commonly used parameters but of relatively high mass can explain the bulk of velocity fluctuations in the plane of the Galactic disk near the Sun. Streaming motions $\approx 10 \text{ km s}^{-1}$ on $\gtrsim 3 \text{ kpc}$ scales in the Milky Way are in good agreement with observations of external galaxies and directly explain why local determinations of the solar motion are inconsistent with global measurements.

Subject headings: Galaxy: disk — Galaxy: fundamental parameters — Galaxy: general — Galaxy: kinematics and dynamics — Galaxy: structure — stars: kinematics

1. INTRODUCTION

One of the major questions in galactic astrophysics is what drives the evolution of large disk galaxies such as the Milky Way (MW). In particular, finding the source of the dependence of the kinematics of stars on age or elemental abundances has been surprisingly difficult. Spitzer & Schwarzschild (1951) presciently suggested that giant molecular clouds can increase the random velocities of stars, while Barbanis & Woltjer (1967) proposed that spiral structure is responsible for this effect. Other proposals include that kinematic heating occurs through encounters with massive black holes (Lacey & Ostriker 1985) or satellite galaxies (Toth & Ostriker 1992; Quinn et al. 1993; Velazquez & White 1999), or that the velocity dispersion at birth of (at least some part of) the disk was high (e.g., Brook et al. 2004; Bournaud et al. 2009; Bird et al. 2013; Stinson et al. 2013). These various mechanisms have so far primarily been tested using observations of the age-

dependence of the velocity dispersion of stars in the solar neighborhood (e.g., Wielen 1977; Nordström et al. 2004) and the ratio of the vertical to the radial velocity dispersion σ_z/σ_R . While the observed density of molecular clouds is too small to produce the observed heating rate and spiral structure is inefficient at generating large vertical velocities (Carlberg 1987; Binney & Lacey 1988), the combination of the two makes predictions that are largely consistent with observations of young and intermediate-age stars. This is because transient spiral structure is efficient at developing large radial velocity dispersions at the observed rate (Carlberg & Sellwood 1985) and scattering of molecular clouds is highly efficient at keeping σ_z/σ_R constant at ≈ 0.5 to 0.6 (Binney & Lacey 1988; Ida et al. 1993; Hänninen & Flynn 2002). However, strong positive evidence for this picture is currently lacking.

Besides spiral structure, the Milky Way is known to host a central bar (Blitz & Spergel 1991; Binney et al. 1991) with a mass of about $10^{10} M_\odot$ (Zhao & Mao 1996; Weiner & Sellwood 1999) and a semimajor axis of about 3 kpc (Binney, Gerhard, & Spergel 1997; Bissantz & Gerhard 2002). The impact of the bar on the kinematics of the stellar disk is typically expected to be small, except near the bar's ends or close to the outer Lindblad resonance, unless the pattern speed changes significantly. The latter is unlikely, as the pattern speed would typically decrease due to dynamical friction (Weinberg 1985) and the Milky Way's bar is almost as fast as it can be given the bar's length (bar corotation should be beyond the bar's semimajor axis; Contopoulos 1980), possibly indicating that it has not significantly slowed down. However, the bar may have

¹ Institute for Advanced Study, Einstein Drive, Princeton, NJ 08540, USA; bovy@ias.edu

² Hubble Fellow

³ John Bahcall Fellow

⁴ Department of Physics and Astronomy, Vanderbilt University, 6301 Stevenson Center, Nashville, TN, 37235, USA

⁵ VIDA Postdoctoral Fellow

⁶ Department of Astronomy, University of Virginia, Charlottesville, VA, 22904, USA

⁷ Instituto de Astrofísica de Canarias, E38205 La Laguna, Tenerife, Spain

⁸ Department of Astronomy, University of Michigan, Ann Arbor, MI, 48104, USA

⁹ Department of Physics and Astronomy, Johns Hopkins University, Baltimore, MD 21218, USA

grown and slowed down simultaneously, thus remaining fast in the above sense (Athanasoula 2003). That the Milky Way’s disk is maximal (Bovy & Rix 2013) also predicts that the bar maintains a large pattern speed for many dynamical times (Debattista & Sellwood 2000). However, depending on the relative location of the bar and spiral resonances, the bar could have a large impact on the heating and migration rate of stars near the Sun (Minchev & Famaey 2010), in particular leading to stronger radial migration than would be produced by spiral structure alone (Sellwood & Binney 2002). Constraining the properties of the bar and the spiral structure is therefore essential for improving our understanding of the evolution of the stellar disk.

Hipparcos (ESA 1997) and more recently the RAVE survey (Steinmetz et al. 2006) have added additional constraints to this picture through observations of the velocity field near the Sun. Dehnen (1998) reconstructed the full local three-dimensional velocity distribution function (DF) in the solar neighborhood from astrometric *Hipparcos* data, revealing a distribution that is far from smooth and is characterized by half a dozen large overdensities or moving groups. Subsequent investigations demonstrated that these systems are likely due to dynamical effects rather than incomplete mixing of newly-formed stars (e.g., Bensby et al. 2007; Famaey et al. 2008; Bovy & Hogg 2010; Sellwood 2010). In particular, De Simone et al. (2004) established that the same type of transient spiral structure that is consistent with the observed heating rate can generate clumps in the local velocity DF. Dehnen (2000) further demonstrated that the action of the central bar on the local stellar disk can create a moving group similar to the Hercules moving group if the Sun is near the bar’s outer Lindblad resonance. More recently, Siebert et al. (2011) and Williams et al. (2013) have performed measurements of the mean velocity field of kinematically-warm stars using RAVE data; they detect a gradient of $\approx -4 \text{ km s}^{-1} \text{ kpc}^{-1}$ in the Galactocentric radial velocity and a complicated pattern of fluctuations not easily explained through a single perturber (but see Faure et al. 2014). Another detection of a non-axisymmetric velocity was reported by Bovy et al. (2012) (hereafter B12), who found that the solar neighborhood is traveling $\sim 14 \text{ km s}^{-1}$ ahead of the circular velocity in their axisymmetric model.

A particular aspect of non-axisymmetric streaming motions is that they may affect determinations of the Milky Way’s circular velocity V_c and of the Sun’s motion relative to V_c . The sum of these—the Sun’s Galactocentric rotational velocity—is crucial for converting observed kinematics from the heliocentric frame to the Galactocentric frame, which is the natural frame for interpreting large-scale kinematics. The precisely measured proper motion of Sgr A* (Reid & Brunthaler 2004) provides a crucial constraint on the Sun’s Galactocentric velocity (assuming that Sgr A* is at rest with respect to the dynamical center of the disk and halo), but the present uncertainty in the value of the distance to the Galactic center means that the uncertainty in the heliocentric-to-Galactocentric coordinate transformation is a serious limiting factor in many analyses of the Milky Way. Various determinations of the Sun’s motion with

respect to V_c based on solar-neighborhood observations (e.g., Dehnen 1998; Schönrich et al. 2010) and larger-scale observations (e.g., B12) differ at the many-sigma level based on their formal uncertainties. This may be due to the unaccounted influence of non-axisymmetry on the kinematics of solar-neighborhood stars.

In this paper we address these issues by exploring the large-scale kinematics of red-clump (RC) stars in the MW disk from the APOGEE survey (Eisenstein et al. 2011; S. R. Majewski et al. 2014, in preparation). The first part of the paper focuses on investigating the large solar motion—defined here as the relative velocity between the Sun and the circular velocity at the solar circle in an axisymmetric approximation of the Milky Way and denoted by $V_{\odot-c}$ ¹⁰—found by B12 but by instead using the RC sample, which is superior to the sample used by B12 because it has much more accurate distances. We find strong evidence in the RC kinematics that the solar motion in the direction of rotation is $V_{\odot-c} \sim 24 \text{ km s}^{-1}$ and therefore that the solar neighborhood is indeed moving $\sim 12 \text{ km s}^{-1}$ faster than the circular velocity. In the second part of the paper, we investigate this result by studying the mean velocity field’s deviations from axisymmetric rotation on scales ranging from 25 pc to 10 kpc. We calculate the power spectrum of fluctuations and find that it exhibits a clear peak at scales corresponding to the response to the central bar.

The outline of this paper is as follows. In § 2 we briefly discuss the various sources of data we employ to study the velocity field on different scales, and § 3 contains our conventions for calculating the two- and one-dimensional power spectrum of velocity fluctuations. We investigate the dependence of the APOGEE-RC kinematics on the assumed solar motion and determine a new value for the solar motion by minimizing the large-scale power in the RC kinematics in § 4. The observed velocity fluctuations on different scales and their power spectrum are presented in § 5.1. We investigate the expected power spectrum for various types of non-axisymmetric perturbations in § 5.2 and identify the central bar as the most plausible agent responsible for the observed fluctuations. We discuss our results in the context of previous findings in § 6 and present our conclusions in § 7. We fix the Sun’s distance to the Galactic center to $R_0 = 8 \text{ kpc}$ throughout our analysis. In this study we calculate Galactocentric coordinates (X_{GC}, Y_{GC}, Z) in a left-handed frame with the Sun at $(X_{GC}, Y_{GC}) = (8, 0) \text{ kpc}$, X_{GC} positive toward $l = 180^\circ$, Y_{GC} increasing toward Galactic rotation, and Z positive toward the North Galactic Pole. In all of the figures, the disk rotates counter-clockwise, that is, it is as seen from the South Galactic Pole.

2. DATA

We primarily use data from the APOGEE survey, but also from RAVE and the Geneva-Copenhagen survey (GCS; Nordström et al. 2004) to investigate velocity fluctuations on smaller scales than is possible with APOGEE. We describe all three data sets briefly in this section.

¹⁰ A perhaps more traditional definition of the solar motion is the motion of the Sun relative to the velocity of a hypothetical stellar population with zero velocity dispersion, which we denote as V_{\odot} . If the Milky Way is axisymmetric then these two definitions agree and $V_{\odot} \equiv V_{\odot-c}$, but more generally they can be different.

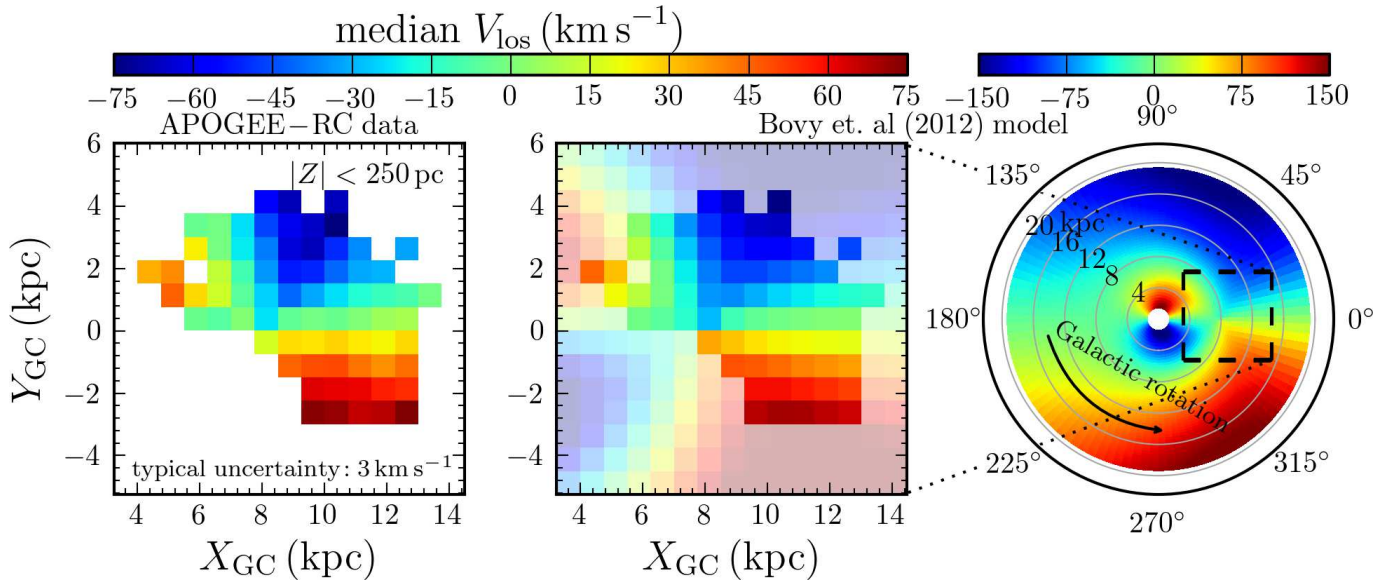


FIG. 1.— Line-of-sight velocity field in the MW out to 5 kpc from the Sun from APOGEE red-clump stars close to the mid-plane (*left panel*). This figure displays the median heliocentric line-of-sight velocity in $(0.75 \text{ kpc})^2$ pixels in rectangular, Galactocentric coordinates. The right panel displays the line-of-sight velocity field over the whole disk obtained in the B12 model for the Milky-Way rotation curve and for the DF of RC stars. The middle panel is an expanded view of the model prediction in the APOGEE volume, with the areas of spatial overlap with APOGEE data highlighted. The velocity color range on the right is twice that in the left and middle panels. The Sun is located at $(X_{GC}, Y_{GC}) = (8, 0)$ kpc.

We use data on the kinematics of RC stars from the DR12 APOGEE-RC catalog, which is constructed using the method described in detail in Bovy et al. (2014), but applied to the DR12 data. Briefly, RC stars are selected from the superset of all APOGEE data in SDSS-III DR12 (C. Ahn et al. 2015, in preparation) using a combination of cuts in the surface-gravity ($\log g$) / effective-temperature (T_{eff}) plane and the $(J - K_s)_0$ / metallicity ($[\text{Fe}/\text{H}]$) plane. These cuts are chosen to select a pure sample of RC stars for which precise luminosity distances can be determined. Reddening and extinction corrections are determined for each star using the Rayleigh Jeans Color Excess method (Majewski et al. 2011); for the RC, random and systematic uncertainties in these corrections are $\lesssim 0.05$ mag (see Bovy et al. 2014). The distance scale is calibrated against an *Hipparcos*-based determination of the RC absolute K_s magnitude in the solar neighborhood (Laney et al. 2012). Corrections to a single absolute magnitude as a function of $([J - K_s]_0, [\text{Fe}/\text{H}])$ based on stellar isochrone models (Bressan et al. 2012) are determined for each star in the catalog individually. The catalog has an estimated purity of $\approx 95\%$ and the distances are precise to 5% and unbiased to 2%. The uncertainty in the line-of-sight velocities is typically 0.1 km s^{-1} . Full details on the APOGEE survey can be found in S. R. Majewski et al. (2015, in preparation), on the APOGEE instrument in Wilson et al. (2010) and J. Wilson et al. (2015, in preparation), on the Sloan 2.5-meter telescope in Gunn et al. (2006), on the APOGEE target selection in Zasowski et al. (2013), on the data reduction pipeline in D. L. Nidever et al. (2015, in preparation), on the stellar-parameters and chemical-abundances analysis in A. E. García Pérez et al. (2015, in preparation), and on the specific DR12 analysis and calibration in J. Holtzman et al. (2015, in preparation).

From the APOGEE-RC catalog we select 8,155 stars

within 250 pc from the Galactic mid-plane. The median heliocentric line-of-sight velocities V_{los} of this sample are displayed in the left panel of Figure 1, which presents the median of the line-of-sight velocities in $(0.75 \text{ kpc})^2$ pixels. All pixels here and in the following figures have a minimum of 20 stars per pixel. The typical uncertainty on the median velocity is 3 km s^{-1} , with smaller values near the Sun and larger values at the far edges of the sample. The observed heliocentric line-of-sight velocity field reflects the combination of the rotation of the Galactic disk and the motion of the Sun with respect to this rotation (see, e.g., B12) and spans a range of $\approx 150 \text{ km s}^{-1}$ in the observed volume. With a typical uncertainty of 3 km s^{-1} , we therefore measure this combination at extremely high signal-to-noise ratio. The right panel of Figure 1 displays the line-of-sight velocity field over the whole Galactic disk obtained for the model of B12, which was fit to the kinematics of stars observed during the first year of APOGEE. The middle panel is an expanded view of the region observed by the APOGEE-RC sample. The residuals between the data and the B12 model are displayed in the top-left panel of Figure 2. The overall agreement between the data and the B12 model is excellent.

We also employ data from the RAVE survey, selecting a sample of RC stars in RAVE by applying almost the same cuts¹¹ applied to create the APOGEE-RC sample to the DR4 RAVE data set (Kordopatis et al. 2013), using the stellar parameters determined by RAVE’s Stellar Parameter Pipeline and dereddening the $J - K_s$ color using $E_{J-K_s} = 0.17 A_V$. We do not perform any other cuts. This approach creates a sample of 30,783 RC stars in RAVE, which have spectra with a typical signal-to-noise

¹¹ We do *not* apply the additional cut in $\log g$ and T_{eff} (equation [9] in Bovy et al. 2014) to RAVE that was necessary for APOGEE because of a relative $\log g$ bias for RC and red-giant stars (see § 2.3 of Bovy et al. 2014).

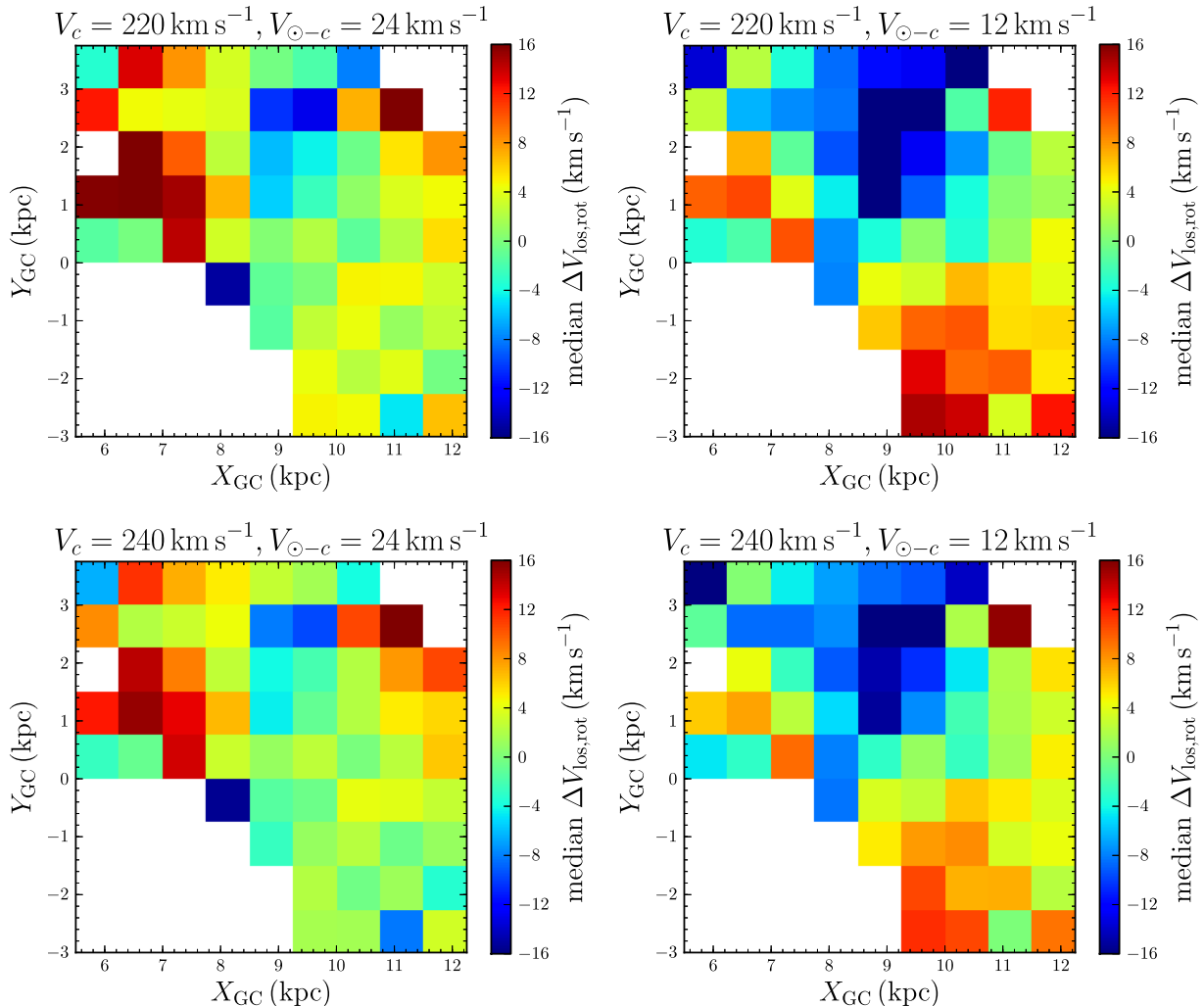


FIG. 2.— Peculiar velocity field in the Milky Way out to 5 kpc from the Sun. These figures display the residuals between the median heliocentric line-of-sight velocities in Figure 1 and the model of B12 (equation [3]), for different values of the circular velocity V_c and the solar motion $V_{\odot-c}$. The peculiar velocity field depends sensitively on the assumed solar motion, but is largely independent of the assumed V_c .

ratio of 50 per resolution element, line-of-sight velocities with uncertainties of typically 1 km s^{-1} , and which are typically within $\approx 2 \text{ kpc}$ from the Sun. For these stars we use the distances from Binney et al. (2014).

Data on the velocity field on small scales is obtained from the GCS catalog (Nordström et al. 2004). We select stars from the GCS catalog that are not flagged as binaries and that have a measured metallicity larger than -1.2 ; 8,123 stars in GCS satisfy these constraints. While for RAVE and APOGEE we use the line-of-sight velocity to investigate the kinematics, for GCS we use the V component of the velocity vector, that is, the y component of the velocity field in the rectangular Galactic coordinate frame. We employ the V component rather than the x component of the velocity field, because it has a smaller dispersion, thus making it easier to determine the median velocity.

3. TWO- AND ONE-DIMENSIONAL POWER SPECTRUM

In § 5 we calculate the power spectrum of the mean velocity field in the Milky Way after subtracting a smooth

axisymmetric model. The power spectrum is a simple, model-independent transformation of the data that, as we argue below, highlights the underlying physical mechanism responsible for non-axisymmetric motions in a powerful manner. We determine the two-dimensional power spectrum and also average the power spectrum azimuthally to determine the one-dimensional power spectrum. As Fourier-transform and power-spectrum conventions are not fully standardized, we briefly discuss our procedure for performing these calculations.

For a two-dimensional field a_{ij} on a rectangular $N \times M$ grid (x_i, y_j) with spacings (Δ_x, Δ_y) , we start by padding each x and each y dimension with $N + 1$ and $M + 1$ zeros, respectively, to avoid periodic pollution in Fourier space (Press et al. 2007). We then calculate the two-dimensional Fourier transformation A_{kl} as

$$A_{kl} = \sum_{i=0}^{2N} \sum_{j=0}^{2M} a_{ij} \exp\left(-\pi I \left[\frac{ik}{N} + \frac{jl}{M}\right]\right). \quad (1)$$

Here, $I = \sqrt{-1}$. We then form the periodogram esti-

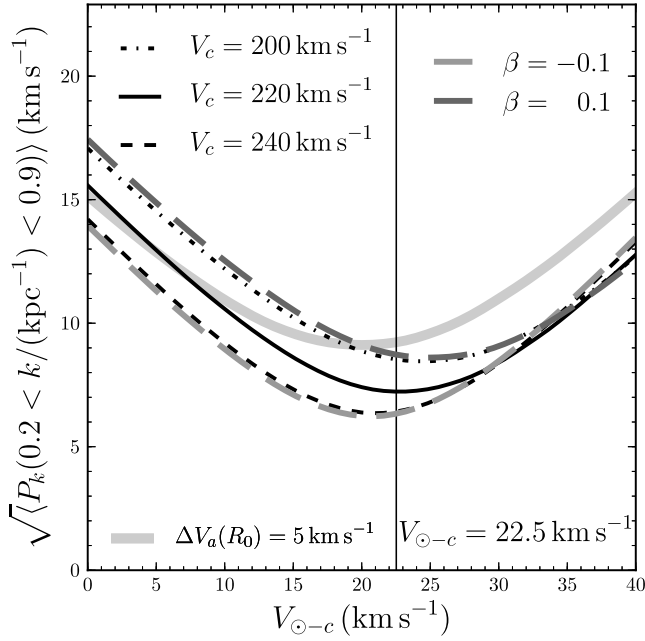


FIG. 3.— Determination of the solar motion by minimizing the large-scale power in the peculiar-velocity field out to 5 kpc. This figure presents the power on scales $0.2 \text{ kpc}^{-1} < k < 0.9 \text{ kpc}^{-1}$ as a function of the solar motion $V_{\odot-c}$ for different models for the MW rotation curve. The power is minimized for the fiducial model of a flat rotation curve with $V_c = 220 \text{ km s}^{-1}$ for a solar motion of $V_{\odot-c} = 22.5 \text{ km s}^{-1}$. Assuming different V_c , a falling or rising rotation curve (parameterized as $V_c(R) \propto R^\beta$ here), or a different asymmetric-drift model (thick gray line, see text) only shifts this minimum by a few km s^{-1} . Simulations indicate that this determination of $V_{\odot-c}$ is biased low by $\approx 1 \text{ km s}^{-1}$ and that it has a random uncertainty of 1 km s^{-1} ; therefore, our value for $V_{\odot-c}$ is $V_{\odot-c} = 24 \pm 1 \text{ km s}^{-1}$.

mate of the two-dimensional power spectrum $P(k_x, k_y)$ (e.g., Press et al. 2007) at frequencies $(k_x, k_y) = (\alpha/N f_x, \beta/M f_y)$, where $\alpha = 0, 1, \dots, N$ and $\beta = 0, 1, \dots, M$. We define $f_x = 1/\Delta_x$ and $f_y = 1/\Delta_y$. This definition is a factor of two larger than that of the Nyquist frequency, but it allows the approximate scale of a fluctuation to be determined as k^{-1} .

We construct the azimuthally-averaged, one-dimensional power spectrum $P(k)$ by averaging $P(k_x, k_y)$ in bins of $k = \sqrt{k_x^2 + k_y^2}$ and multiplying by $(4\pi)^2$

$$P(k) = \frac{(4\pi)^2}{N_k} \sum_{(k_x, k_y) \text{ in bin } k} P(k_x, k_y), \quad (2)$$

where N_k is the number of points in the (k_x, k_y) grid that fall within the k bin.

4. A NOVEL, GLOBAL DETERMINATION OF THE SOLAR MOTION

The two-dimensional velocity field of heliocentric line-of-sight velocities in Figure 1 can be modeled as arising from the combination of three elements: (a) the overall differential rotation of the Galactic disk (i.e., the circular-velocity curve), (b) the offset between the mean velocity of the population of RC stars and circular rotation (i.e., the asymmetric drift), and (c) the Sun’s motion with

respect to the Galactocentric restframe. We do not attempt to fully model all of these ingredients here; instead, we adopt the best-fit model from B12, which consists of a model for the MW potential (a simple power-law rotation curve) and for the stellar DF, assumed to be axisymmetric and well-mixed. This model was fit to the kinematics of a sample of stars at fourteen $b = 0^\circ$ fields in the first year of APOGEE data, by approximating the two-dimensional DF of these stars as a bivariate Gaussian with a mean rotational-velocity offset from circular rotation given by a simple asymmetric-drift model and constant radial anisotropy.

The model in B12 was fit to all types of stars in APOGEE—not only RC stars, but also first-ascent red giants and dwarfs. Only 782 of the 8,155 stars that we select here from the APOGEE-RC sample were part of the sample of 3,365 stars used in the B12 analysis. Therefore, the samples are largely independent. The B12 sample extends to larger distances, because it includes luminous red giants up to $(J - K_s)_0 = 1.1$. For this reason the B12 sample was more suited for determining the parameters of the circular velocity curve and in particular for the circular velocity at the Sun itself. We thus keep most of the parameters of the B12 model fixed for the RC sample used in this paper and focus our attention on the solar motion in the rotational direction. We set the radial-velocity dispersion of the Gaussian DF model to 31.4 km s^{-1} , the radial scale length of the population to 3 kpc, and we fix the velocity-dispersion profile to be flat. The Sun’s radial motion $V_{R,\odot}$ is fixed to -10.5 km s^{-1} and the Sun’s vertical velocity $V_{Z,\odot}$ is set to 7.25 km s^{-1} (Schönrich et al. 2010).

With these parameter selections we can compute the expected mean velocity at the location of each RC star in our sample. We calculate the peculiar velocities $\Delta V_{\text{los,rot}}$ with respect to the mean model prediction at a point with Galactocentric cylindrical coordinates (R, ϕ)

$$\begin{aligned} \Delta V_{\text{los,rot}}(R, \phi) = & V_{\text{los}} / \cos b - V_{R,\odot} \cos l \\ & + [V_c(R_0) + V_{\odot-c}] \sin l + V_{Z,\odot} \sin b / \cos b \\ & - [V_c(R) - V_a(R)] \sin(l + \phi), \end{aligned} \quad (3)$$

where $V_a(R)$ is the asymmetric drift. By taking the median of these values we can determine the peculiar velocity field in the MW disk, which should be zero if the disk is axisymmetric.

The peculiar velocity field calculated assuming a flat rotation curve with $V_c = 220 \text{ km s}^{-1}$ and a solar motion $V_{\odot-c} = 24 \text{ km s}^{-1}$ is displayed in the top left panel of Figure 2. The deviations from zero are large ($\sigma \approx 7 \text{ km s}^{-1}$), but on average the deviation is close to zero. The top right panel demonstrates the velocity field using what is currently considered as the standard solar motion, $V_{\odot-c} = 12 \text{ km s}^{-1}$ (determined from solar neighborhood kinematics and therefore assuming that $V_{\odot-c} \equiv V_\odot$; Schönrich et al. 2010). In this case, a large-scale systematic trend is visible in the peculiar velocity field. The bottom panels of Figure 2 illustrate that this conclusion is largely independent of the assumed value for V_c : for $V_c = 240 \text{ km s}^{-1}$, similar patterns exist in the peculiar velocity field. This is the case because the mean

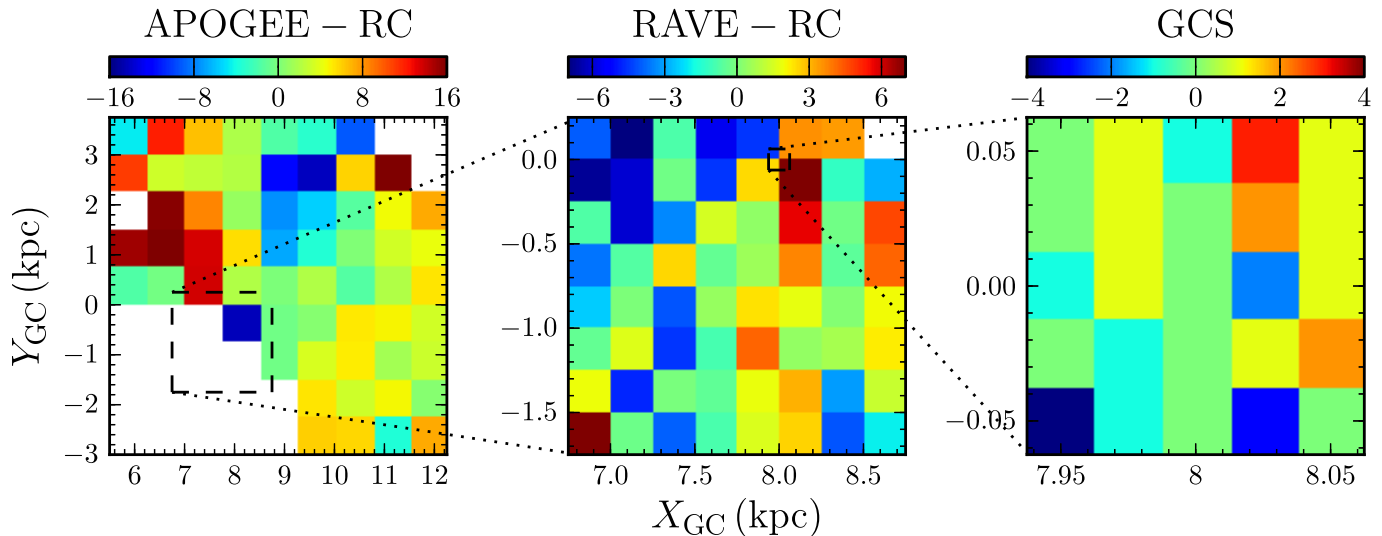


FIG. 4.— Peculiar velocity field on different scales in the MW. This figure displays the MW’s peculiar-velocity field in km s^{-1} on scales ranging from 25 pc to 10 kpc by combining three different surveys. The rightmost panel shows the fluctuations in the V component of the velocity of GCS stars, in $(25 \text{ pc})^2$ pixels in a box of size $(125 \text{ pc})^2$ around the Sun. The middle panel displays the peculiar velocity field of RAVE red-clump stars, in $(250 \text{ pc})^2$ pixels covering a square of size $(2 \text{ kpc})^2$ around the Sun. The leftmost panel presents the peculiar velocity field in $(0.75 \text{ kpc})^2$ pixels out to 5 kpc (the same as the top, left panel of Figure 2, but using $V_{\odot-c} = 22.5 \text{ km s}^{-1}$ to minimize the large-scale power). The color scale ranges over a smaller range in velocities in the middle and right panels. There is a clear increase in the amplitude of the velocity fluctuations from the smallest to the largest scales.

line-of-sight velocity field \bar{V}_{los} assuming axisymmetry is given by

$$\bar{V}_{\text{los}} = [V_c(R) - V_a(R)] \sin(\phi + l) - [V_c(R_0) + V_{\odot-c}] \sin l, \quad (4)$$

where for simplicity we have assumed that the Sun’s radial motion is zero. For a close-to-flat rotation curve ($V_c(R) \approx V_c(R_0)$) and a narrow range in ϕ , this expression reduces to

$$\bar{V}_{\text{los}} \approx [V_c - V_a(R)] \sin \phi \cos l - [V_a(R) + V_{\odot-c}] \sin l, \quad (5)$$

The dependence on V_c is $\propto \sin \phi \cos l$ and because of the narrow ϕ range is therefore quite weak (typical $|\phi| \approx 12^\circ$, so typical $|\sin \phi| \approx 0.2$) while the dependence on $V_{\odot-c}$ is $\propto \sin l$ and thus strong (we vary both V_c and $V_{\odot-c}$ over 40 km s^{-1}). As we discuss in § 6.2 below, the difference in the inferred $V_{\odot-c}$ value here and that based on more local observations can be explained by the difference in the survey volumes used in the measurements.

To determine quantitatively for which $V_{\odot-c}$ the large-scale trend in the peculiar velocity field is minimized we compute the one-dimensional power spectrum using the method described in the previous section. This power spectrum is discussed in more detail in the next section. For this application, we note that most of the power is contained in the interval $0.2 \text{ kpc}^{-1} < k < 0.9 \text{ kpc}^{-1}$. We can ask for what value of $V_{\odot-c}$ this power is minimized, that is, which value of $V_{\odot-c}$ minimizes large-scale power in the peculiar velocity field. This is similar to asking what axisymmetric model for disk kinematics best reproduces the observations. Figure 3 presents the average power on scales $0.2 \text{ kpc}^{-1} < k < 0.9 \text{ kpc}^{-1}$ as a function of the assumed $V_{\odot-c}$, for different values of V_c for a flat rotation curve and for a rising and falling rotation curve with $V_c(R_0) = 220 \text{ km s}^{-1}$. We also show the effect of using a different model for the stellar DF that results in a different asymmetric drift: the thick gray

line assumes that the scale length of the exponential decline of the velocity dispersion is 8 kpc (rather than the flat fiducial profile). This model leads to an asymmetric drift that is different by $\Delta V_a = 5 \text{ km s}^{-1}$ at R_0 and has the opposite radial dependence (see the bottom panel of Figure 4 of B12; this model was strongly disfavored by the data in that paper). For all of the different assumptions about the rotation curve and stellar DF the power is minimized for $20 \text{ km s}^{-1} < V_{\odot-c} < 25 \text{ km s}^{-1}$. For a flat rotation curve with $V_c = 220 \text{ km s}^{-1}$ the minimum occurs at $V_{\odot-c} = 22.5 \text{ km s}^{-1}$.

To understand potential biases and the random uncertainty associated with this estimate, we have performed Monte Carlo simulations of the velocities of the RC sample using an axisymmetric Dehnen stellar DF (Dehnen 1999) with $\sigma_R = 31.4 \text{ km s}^{-1}$, a scale length $h_R = 3 \text{ kpc}$, and a flat dispersion profile in a flat-rotation curve potential with $V_c = 220 \text{ km s}^{-1}$. The simulated velocity in these simulations is generated at the catalog position of each RC star; because we are using sub-kpc pixels and the distance uncertainties are much smaller than this, selection and distance-error effects are negligible for this exercise. For each of 100 simulated samples we determine $V_{\odot-c}$ in the same manner as for the data, assuming a true $V_{\odot-c}$ of 24 km s^{-1} . These simulations reveal that the estimate for $V_{\odot-c}$ is biased low by $\approx 1 \text{ km s}^{-1}$ and has a random uncertainty of 1 km s^{-1} . The bias is most likely due to the Gaussian approximation for the velocity distribution, which in reality is skewed toward lower rotational velocities. We have also performed similar Monte Carlo simulations where the velocity field is adjusted according to the non-axisymmetric response to the central bar (with the parameters that we favor in § 5 below). Even in this non-axisymmetric case, $V_{\odot-c}$ as determined by the present procedure is affected by less than 1 km s^{-1} . Therefore, our best estimate is $V_{\odot-c} = 24 \pm 1 \text{ km s}^{-1}$.

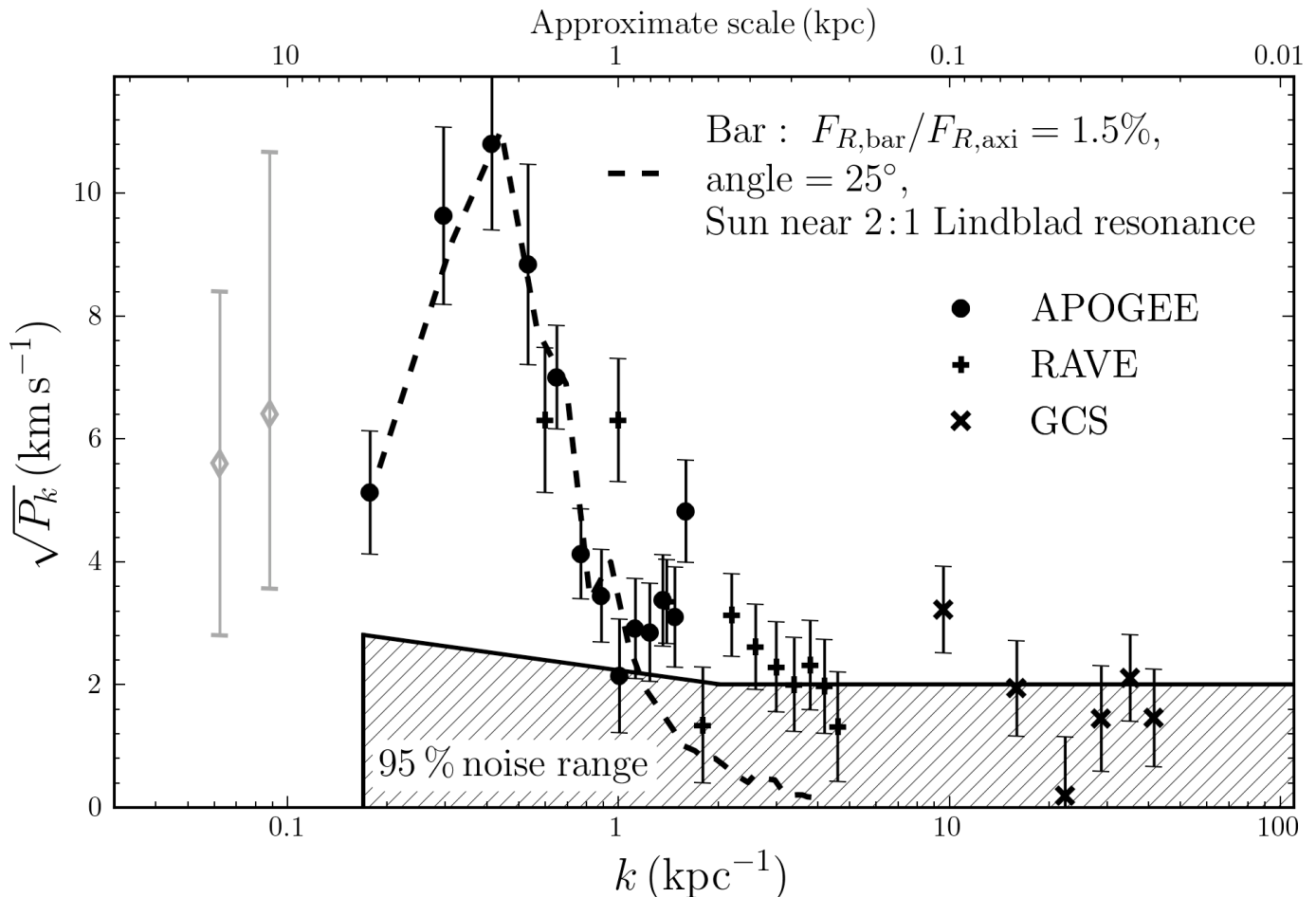


FIG. 5.— One-dimensional power spectrum of velocity fluctuations in the MW disk computed from the APOGEE (filled dots), RAVE (plusses), and GCS (crosses) velocity fields shown in Figure 4. We have subtracted the median noise power spectrum to display the intrinsic fluctuations; the hatched region displays the region that contains 95% of the noise. Most of the power is on scales $0.2 \text{ kpc}^{-1} < k < 0.9 \text{ kpc}^{-1}$. Inspection of the full two-dimensional power spectrum establishes that this power is almost entirely contained within $|\Delta k| = 0.1$ of $(k_x, k_y) = (0.4, -0.15)$ —that is, mainly radial—with a tail to $k_y = 0.25$ at fixed k_x (all k are in kpc^{-1}). The gray points on the largest scales are estimates of the power on even larger scales from observations of external disk galaxies (Rix & Zaritsky 1995). The dashed line shows the expected power spectrum from the response to the central bar (see text for details), which can explain the peak in the power spectrum. On smaller scales ($k \gtrsim 1 \text{ kpc}^{-1}$), the observed power spectrum is consistent with measurement noise.

A 20 km s^{-1} higher or lower V_c shifts $V_{\odot-c}$ by about 2 km s^{-1} and a similar move happens for a gently rising or falling rotation curve, so a rather conservative systematic uncertainty on $V_{\odot-c}$ due to incomplete knowledge of $V_c(R)$ is 2 km s^{-1} . We discuss the influence on $V_{\odot-c}$ of non-axisymmetric motions on scales larger than those observed here in § 6.2.

5. THE POWER SPECTRUM OF VELOCITY FLUCTUATIONS

5.1. Observations

Having subtracted an axisymmetric model for the heliocentric line-of-sight velocities in the mid-plane of the MW disk, we can now study the peculiar velocities. On the large scales traced by APOGEE, these are presented in the left panel of Figure 4. The peculiar velocities have a standard deviation of about 10 km s^{-1} , much larger than the uncertainty on the mean peculiar velocity in each pixel, which is typically 3 km s^{-1} . To investigate the properties of the peculiar velocity field on scales $\lesssim 1 \text{ kpc}$ that we cannot resolve well currently with APOGEE, we use the data from RAVE and the GCS in the solar

neighborhood described in § 2. These observations are displayed in the middle and right panel of Figure 4, respectively. For the RAVE RC stars we use the same axisymmetric model as for APOGEE, except that we adopt $V_{\odot-c} = 10 \text{ km s}^{-1}$, as this value better fits the RAVE kinematics (Sharma et al. 2014). We discuss this discrepancy between the global $V_{\odot-c}$ that we employ for APOGEE and the local value that we adopt for RAVE in much more detail in § 6.2. For GCS we simply plot the median V velocity from the GCS catalog, because there are no Galactic gradients in the $\approx (100 \text{ pc})^2$ covered by the GCS sample. This figure illustrates that the peculiar motions are mainly confined to large scales, because the range of velocities covered by the color scale is a factor of two and four smaller for the middle and right panels, respectively, compared to the left panel. On the sub-kpc scales probed by RAVE and GCS, peculiar velocities are uniformly small.

To better quantify this behavior, we calculate the two-dimensional power spectrum of the fluctuations shown in Figure 4. The one-dimensional, azimuthally-averaged power spectrum is shown in Figure 5. In detail, this one-

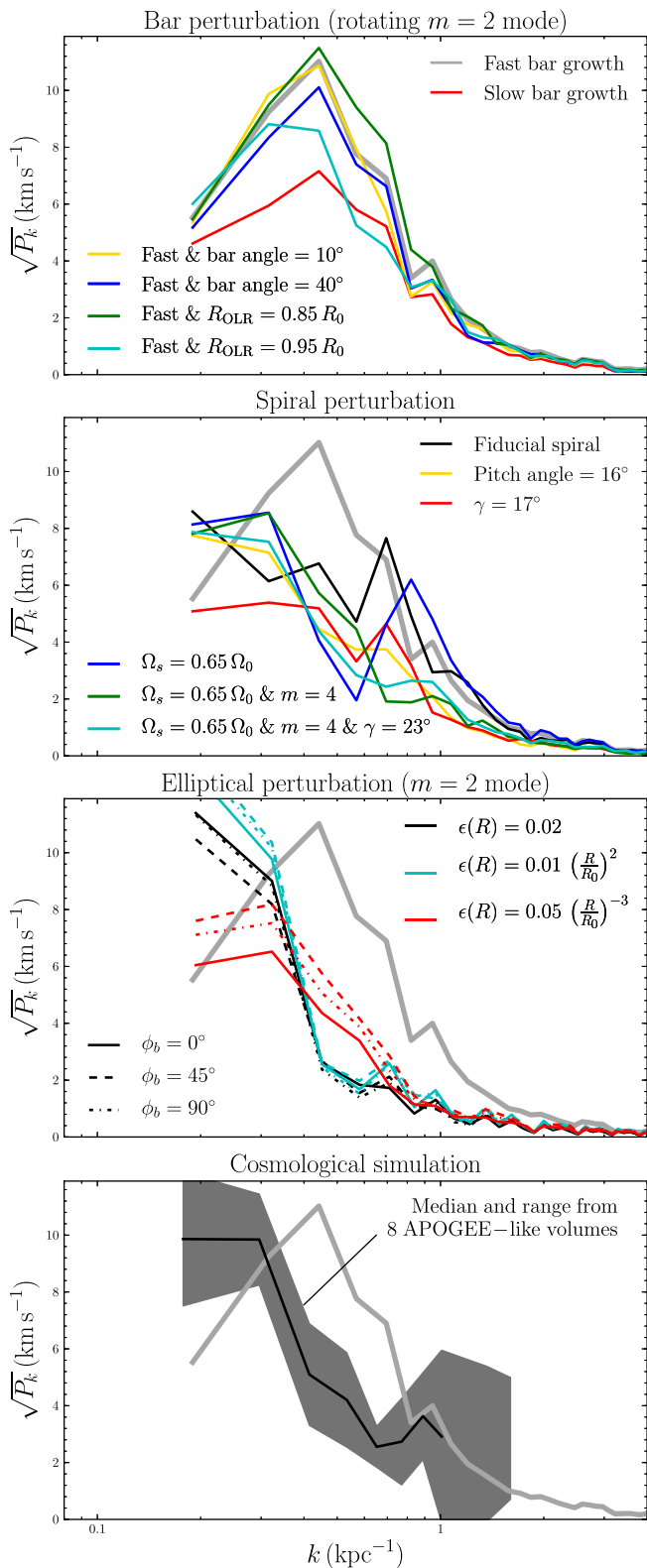


FIG. 6.— Model power spectra for different non-axisymmetric modes: (a) bar modes, (b) spiral modes with various parameters, (c) elliptical modes, and (d) the power spectrum in the cosmological simulation from Guedes et al. (2011). The various models are explained in detail in § 5.2. The fiducial bar model (thick gray line in all panels) fits the observed data as demonstrated in Figure 5. A bar is the most plausible explanation for the observed peak in the power spectrum in Figure 5.

dimensional power spectrum is obtained by following the procedure in § 3 for the APOGEE, RAVE, and GCS velocity fields in Figure 4 separately; we do not display the smallest k and the three largest k for each data set to minimize pixelization effects. For each data set we perform 1,000 Monte Carlo simulations of the noise by generating Gaussian random fields scaled to the measurement uncertainty on $\Delta V_{\text{los,rot}}$ in observed pixels and we calculate their power spectrum in the same manner. We subtract the median of these 1,000 noise power spectra from the data and indicate the 95% noise range determined from these simulations. All power above this 95% noise range is therefore detected at 2σ . The combination of the three data sets allow a measurement of the one-dimensional power spectrum on all scales in the range $0.2 \text{ kpc}^{-1} \leq k \leq 40 \text{ kpc}^{-1}$, excluding only the largest spatial scales in the disk. As an estimate of the expected power on even larger scales, we include the typical power in elliptical and lopsided modes for MW-like galaxies from Rix & Zaritsky (1995). If we change the value of $V_{\odot-c}$ used for the APOGEE-RC sample or if we modify the parameters of the asymmetric-drift model, the only change is that the height of the peak becomes larger (reflecting the fact that the axisymmetric fit becomes worse; see Figure 3), but the shape of the power spectrum remains the same. As noted by Binney et al. (2014), the RAVE RC distances that we employ may be underestimated by ≈ 0.08 mag. We have repeated the power-spectrum analysis using 4% larger RAVE distances and find no qualitative impact on the observed power spectrum.

The observed power spectrum is characterized by a single large peak on scales $0.2 \text{ kpc}^{-1} \lesssim k \lesssim 0.9 \text{ kpc}^{-1}$. The power on scales smaller than 1 kpc ($k \gtrsim 1 \text{ kpc}^{-1}$) is consistent with being noise in the measurement of $\Delta V_{\text{los,rot}}$. This result is entirely expected for the kinematically-warm populations of stars in our three samples. Any inhomogeneity on small scales would tend to be washed out by epicyclic motions. Interestingly, the power declines for the two smallest k measured by APOGEE. This behavior indicates that most of the power in the peculiar velocities in the MW (at least in the region surveyed by the APOGEE-RC sample) is on the $\approx 2 \text{ kpc}$ scales where the power spectrum peaks. Extrapolating this behavior, we therefore expect that future investigations of peculiar velocities on larger scales will find relatively little power in, e.g., elliptical or lopsided modes. Using the lack of azimuthal variations in the metallicity distribution in the APOGEE-RC sample as a constraint, Bovy et al. (2014) already limited elliptical modes to streaming motions $\lesssim 10 \text{ km s}^{-1}$, although these constraints and equivalent constraints on lopsided modes will become significantly better with future data from APOGEE-2, the second phase of the APOGEE project, which will operate from 2014 to 2020 and which will (sparsely) cover the entire disk (Sobeck et al. 2014).

An investigation of the two-dimensional power spectrum demonstrates that most of the power is in fact in a single peak around $(k_x, k_y) = (0.4, -0.15) \text{ kpc}^{-1}$, or largely in the x direction. The line-of-sight projection effects and incomplete spatial sampling make it difficult to interpret the two-dimensional power spectrum. We only model the one-dimensional power spectrum below,

because of these difficulties and also because the two-dimensional measurement is noisier.

The peak in the power spectrum occurs at $k \approx 0.5 \text{ kpc}^{-1}$, meaning that the largest variations in the peculiar velocity field are on $\approx 2 \text{ kpc}$ scales, using our frequency definitions in § 3. Among likely culprits, such a peak can be accurately reproduced by the response to a central bar. An illustrative model for the response of the disk to the bar that fits the observed peak is overlaid in Figure 5. This bar has an angle of 25° with respect to the Sun–Galactic-center line, a pattern speed of $\Omega_b = 1.9 \Omega_0$ (where Ω_0 is the local rotational frequency), and a radial-force-amplitude at R_0 of 1.5% relative to the axisymmetric force. We discuss this and alternative models further in the next subsection.

5.2. Modeling of non-axisymmetric perturbations

To interpret the measurement of the power spectrum of velocity fluctuations, we perform simulations of the effect on the velocity field of various non-axisymmetric perturbations to the Galactic potential, using the backward-integration technique of Dehnen (2000). For an assumed non-axisymmetric perturbation, this method finds the value of the stellar DF at a given phase-space point today by reverse integration of the orbit until a time t_0 before the non-axisymmetric was active; the DF today is then equal to the axisymmetric DF at t_0 evaluated at the position of the orbit at t_0 . Specifically, we make use of the `evolveddiskdf` implementation of this method in `galpy`¹² (Bovy 2015). The spatial dependence of the mean velocity response for the perturbations considered below is similar to that of a kinematically-cold population, as expected from linear perturbation theory (Binney & Tremaine 2008). However, analytically calculating the amplitude of the kinematically-warm response is in general difficult.

All of the simulations below assume a background potential with a flat rotation curve and an initial DF given by a Dehnen DF (Dehnen 1999) with $\sigma_R = 31.4 \text{ km s}^{-1}$, a scale length $h_R = 3 \text{ kpc}$, and a flat dispersion profile (these properties do not change considerably due to the non-axisymmetric perturbation). We compute the mean peculiar velocity field over $5.5 \text{ kpc} \leq X_{GC} \leq 12.25 \text{ kpc}$ and $-3 \text{ kpc} \leq Y_{GC} \leq 3.75 \text{ kpc}$ (the range of the data, see Figure 2) by computing moments of the non-axisymmetric DF and then determine its power spectrum in the same way as for the data. The slope of the rotation curve has only a sub-dominant effect on the power spectrum for all of the perturbations considered below and we therefore only discuss the flat-rotation curve.

The result of these simulations are displayed in the top two panels of Figure 6. The top panel has the results for a central bar, modeled as a simple quadrupole with the same parameters as those of Dehnen (2000), except that the bar is 50% stronger, with a radial-force-amplitude at R_0 of 1.5% relative to the axisymmetric force (see the end of the previous section for the full set of bar parameters). The gray curve demonstrates the effect of a bar that is grown over two bar periods and subsequently evolved for two more bar periods (the default model of Dehnen 2000). The red curve displays the effect of an

adiabatically-grown bar; this bar was grown over 68 bar periods and evolved for 7 more periods. The resulting velocity power spectrum is similar for these two cases, but the more slowly-grown bar gives rise to smaller velocity fluctuations with a somewhat flatter spectrum on large scales. We also investigate variations in the bar’s angle and pattern speed; these do not strongly affect the shape of the power spectrum, except for the slower bar.

The second panel in Figure 6 demonstrates the effect of a logarithmic spiral potential with various parameters. The fiducial spiral model is that of an $m = 2$ spiral with a pitch angle of 8° , a pattern speed of $\Omega_s = 0.33 \Omega_0$ that puts the Sun close to the 2 : 1 inner Lindblad resonance, and an angle γ (between the Sun–Galactic-center line and the line connecting the Galactic center to the peak of the spiral pattern at R_0) of 69° . The other curves display the effect of variations in these parameters: (a) a larger pitch angle, (b) a different angle γ , (c) a larger pattern speed that puts the Sun near the 4 : 1 inner Lindblad resonance, (d) an $m = 4$ spiral with the latter pattern speed, and (e) case (d) with a different angle γ . While the power spectrum of the velocity response to these different spiral perturbations varies, it typically places most of the power on the largest scales in a way that is inconsistent with the observed data, such that spiral structure alone cannot explain the observed power spectrum.

The third panel of Figure 6 shows the power spectrum of velocity fluctuations induced by an elliptical perturbation, that is, a perturbation to the potential $\propto \epsilon(R) \cos 2[\phi - \phi_b]$ (see, e.g., Kuijken & Tremaine 1994). Such a perturbation could result from, e.g., a triaxial halo. Rather than fully simulating the response in the manner described above, we make use of the results of Bovy (2015), who characterized the radial- and rotational- velocity response of a kinematically-warm stellar disk to an elliptical perturbation in detail using the backward-integration technique. Bovy (2015) found that the response is well characterized by the response of a cold disk, which can be computed analytically, multiplied by reduction factors $\mathcal{F}_{V_R}(\sigma_R)$ and $\mathcal{F}_{V_T}(\sigma_R)$ for the radial and rotational velocity, respectively. The different colors in the third panel of Figure 6 demonstrate the response for different radial dependencies of $\epsilon(R)$ and the line-styles show the effect of varying the angle ϕ_b . As expected, regardless of the detailed form of the ellipticity, the power spectrum always peaks on the largest scales, with little power on the scales where the observed power spectrum peaks.

Finally, we investigate velocity fluctuations in a high-resolution cosmological simulation. In particular, we examine ErisLE (as described in Bird et al. 2013), a member of the Eris simulation suite designed to follow the formation of Milky-Way-sized galaxies. Several key structural and kinematic properties of this simulated galaxy, which closely resemble those of the Milky Way at $z = 0$, have been studied extensively in Guedes et al. (2011), Guedes et al. (2013), and Bird et al. (2013). To mimic the APOGEE observations, we calculate the mean velocity $\bar{V}(R)$ as a function of radius using all stars at l $30^\circ \leq l \leq 210^\circ$, $|b| \leq 1.5^\circ$, and height $|z| \leq 0.25 \text{ kpc}$ from a Sun-like position in the simulation (i.e., at 8 kpc from the center). We compute the residuals between the median velocity field of stars with ages between 1 and

¹² <http://github.com/jobovy/galpy> .

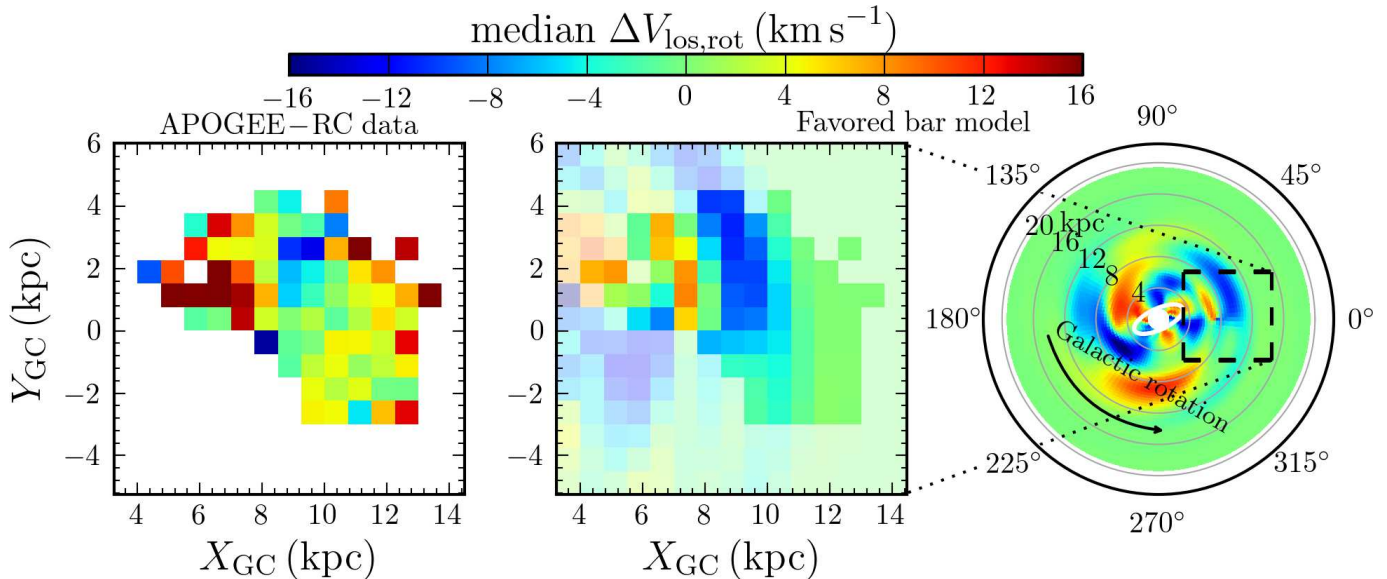


FIG. 7.— The observed peculiar line-of-sight velocity field (*left panel*) compared to that in the bar model favored in this paper. The right panel displays the peculiar line-of-sight velocities induced by the bar over the whole Galactic disk and the middle panel expands the region currently observed by APOGEE. The bar’s orientation and extent are indicated by the white ellipse in the right panel. The model explains some of the large-scale features (positive velocities near $(X_{\text{GC}}, Y_{\text{GC}}) = (7, 2)$ kpc; negative velocities at $X_{\text{GC}} \approx 9$ kpc, $0 < Y_{\text{GC}} < 4$ kpc), but it has almost no response at $R \gtrsim 11$ kpc. The difficulty of detecting the effect of the bar in the velocity field itself demonstrates why the power spectrum is a much more sensitive tool than the velocity field itself for determining the most important non-axisymmetric actor(s).

5 Gyr (to mimic the RC population) and the velocity field $\bar{V}(R)$. This procedure is repeated for 8 different Sun-like positions. The bottom panel of Figure 6 displays the median power spectrum of these 8 positions as well as the 1σ range. The velocity fluctuations in the cosmological simulations are of a similar magnitude as those observed in the data, but they are typically found on the largest scales in the APOGEE-like volume. Direct inspection of the cosmological simulation reveals that the velocity perturbations are most likely generated by spiral structure, which is apparent in the projected surface density, because the simulated galaxy has not experienced a recent major merger nor is the transient, large-scale bar prominent over the last 5 Gyr (the strength of the bar in ErisLE gradually decreases during this time, likely due to a combination of dynamical friction and gas inflow; Debattista et al. 2006; Guedes et al. 2013). The power spectrum of velocity fluctuations is consistent with this interpretation, as it is more like that of the simple spiral simulations than that of the bar, but it is inconsistent with the APOGEE observations.

6. DISCUSSION

6.1. Non-circular motions in the MW

After subtracting our best smooth, axisymmetric model for the kinematics of APOGEE-RC stars, large peculiar velocities on scales $\gtrsim 1$ kpc exist. Variations in the peculiar velocities on the smaller scales observed in the RAVE and GCS samples are absent, at least in the solar neighborhood. These results are in qualitative agreement with the amplitude of $\approx 10 \text{ km s}^{-1}$ of the observed wiggles in the terminal velocities of HI/CO in the MW (e.g., Levine et al. 2008) or in the peculiar velocity field in external galaxies (e.g., Visser 1980), which occur on similar scales, but have usually been interpreted as being due to spiral structure (e.g., Yuan 1969; Burton 1971). That there are large-scale streaming motions at

the amplitude that we observe is therefore not surprising, but it is the first time that these motions are measured at high signal-to-noise ratio in the intermediate-age stellar component.

As is clear from Figure 5 and § 5.2, the observed power spectrum of velocity fluctuations can be accurately modeled as being the response to the central bar and this is the likeliest non-axisymmetric mode that can explain the observations. A radial-force-amplitude at R_0 of 1.5% relative to the axisymmetric force corresponds to a bar mass of $\approx 1.5 \times 10^{10} M_{\odot}$, well within the range of other estimates of the bar mass (e.g., Dwek et al. 1995; Zhao & Mao 1996; Weiner & Sellwood 1999). Figure 7 directly compares the observed peculiar-velocity field to that in the favored bar model: the left panel displays the observed peculiar-velocity field, the right panel shows the model over the whole Galactic disk, and the middle panel expands the region currently observed by APOGEE. It is clear that the model reproduces some of the qualitative features of the observed peculiar velocities, although the data exhibit larger fluctuations than those due to the bar, especially at $R \gtrsim 10$ kpc.

The bar model makes strong predictions for the peculiar velocity field that can be determined from future APOGEE-2 data in the Southern Hemisphere ($l \geq 210^{\circ}$) or in the outer Milky Way: at $R \gtrsim 11$ kpc the bar should have almost no perceptible effect on the stellar velocity distribution. APOGEE-2 will also be able to constrain the bar further by observations of the whole velocity distribution rather than just its mean (Bovy 2010).

That the bar is successful at explaining the observed distribution of power in the peculiar velocity field does not necessarily mean that the effect of other non-axisymmetric modes is negligible. We almost certainly require additional non-axisymmetry to explain the $\approx 4 \text{ km s}^{-1}$ positive line-of-sight velocities at $R \gtrsim 10$ kpc in the data (see Figure 7). While it is clear from Fig-

ure 6 that the observed power spectrum places tight constraints on elliptical perturbations, spiral structure at levels that can have significant heating and migration effects are still possible. Future investigations in regions of the disk where the effect of the bar is small (e.g., the disk at $R \gtrsim 11$ kpc) or on much larger scales ($k \lesssim 0.2$ kpc $^{-1}$) can be used to determine the parameters and likely effect of spiral structure. Truly global investigations of the velocity field, however, will be necessary for this.

6.2. The global and local solar motion

Having characterized the spectrum of velocity fluctuations, we can return to the question of why the solar motion $V_{\odot-c}$ measured by APOGEE is so much larger than that measured locally and which we denote by V_{\odot} . Analyses of the local kinematics of stars in *Hipparcos* (Dehnen & Binney 1998; Hogg et al. 2005), GCS (Binney 2010; Schönrich et al. 2010), or RAVE (Sharma et al. 2014) all find that $V_{\odot} = 5$ to 12 km s $^{-1}$, with the latter value being considered to be more accurate because of unmodeled correlations between the color used to define populations of stars and the populations' radial gradients in the former. A direct examination of the GCS catalog shows that the local value V_{\odot} cannot be much larger than 12 km s $^{-1}$, because otherwise all of the stars in the solar neighborhood are at their pericenters, a result that would be at odds with everything that is known about galactic disks and the MW disk in particular. However, the way the local V_{\odot} is measured implies that V_{\odot} is the solar motion with respect to a hypothetical zero dispersion population at the position of the Sun. If the whole solar neighborhood is participating in a global streaming motion, then there will be an offset between the local V_{\odot} and the global $V_{\odot-c}$, the latter defined as the difference between the Sun's rotational velocity and the axisymmetric V_c (e.g., Shuter 1982; Kuijken & Tremaine 1994; Metzger et al. 1998). This issue is discussed in detail in B12.

Our new measurement of the peculiar velocity field proves that it is indeed likely that the solar neighborhood is affected by a streaming motion of $V_{\odot-c} - V_{\odot} \approx 10$ km s $^{-1}$. The power spectrum of velocity fluctuations demonstrates that such fluctuations are common on scales of $\gtrsim 1$ kpc, while there is little power on smaller scales. This result directly explains why all local surveys, which are limited to distances projected onto the plane $\lesssim 1$ kpc measure the same V_{\odot} : They are all affected by—and are insensitive to—the same streaming motion.

The global value of $V_{\odot-c} = 24$ km s $^{-1}$ that we determined in this paper uses the largest scales in the sample and is therefore less affected by large-scale streaming motions. This value was first obtained by B12 using the first year of APOGEE data. Because that analysis used more luminous and hence more distant red giants than the RC stars used here, it determined $V_{\odot-c}$ on even larger scales. The fact that the power spectrum turns over around $k \approx 0.5$ kpc $^{-1}$ implies that there is little power on the largest scales. Therefore, the global value of $V_{\odot-c}$ measured here and in B12 will not suffer from the large streaming-related systematics that the local V_{\odot} experience. Conservatively, we can assign the amplitude of the velocity power measured at the largest scale in our sample— ≈ 5 km s $^{-1}$ at $k = 0.16$ kpc $^{-1}$ —as

a systematic uncertainty on the global value of $V_{\odot-c}$. Determinations of the Sun's velocity on larger scales than those considered here, for example, by modeling the kinematics of tidal streams, are also global measurements and are by and large consistent with our measurement. For example, the large solar velocity with respect to the Galactic center obtained from the Sgr stream (Carlin et al. 2012) is consistent with our $V_{\odot-c}$ combined with $V_c \approx 220$ km s $^{-1}$.

The streaming motion of 12 km s $^{-1}$ of the whole solar neighborhood must be caused by a non-axisymmetric perturbation. The bar model favored above to explain the RC peculiar velocity field includes a rotational streaming motion at the Sun of ≈ 4 km s $^{-1}$ (using equation [14] of Mühlbauer & Dehnen 2003), which falls short of explaining the observed streaming motion by 8 km s $^{-1}$. This discrepancy would only be 6 km s $^{-1}$ if the bar angle were 10° . Nevertheless, an additional streaming motion induced by a different non-axisymmetric agent, such as spiral structure, is probably necessary to explain the large streaming motion of the solar neighborhood.

With $V_{\odot-c} = 24$ km s $^{-1}$ and the measured proper motion of Sgr A* of 30.24 km s $^{-1}$ kpc $^{-1}$ (Reid & Brunthaler 2004),

$$V_c = 218 \text{ km s}^{-1} + 30.24 \text{ km s}^{-1} \text{ kpc}^{-1} (R_0 - 8 \text{ kpc}) . \quad (6)$$

Therefore, for $R_0 = 8$ kpc, this measurement of V_c agrees perfectly with the measurement of B12. That determination uses a largely different stellar sample and does not include the Sgr A* proper motion, so this agreement is a genuine consistency check on both analyses. To increase V_c to > 240 km s $^{-1}$ requires that $R_0 > 8.7$ kpc, which is highly unlikely given the current best constraints (Ghez et al. 2008; Gillessen et al. 2009). Equation (6) is not entirely correct, as Figure 3 demonstrates that the $V_{\odot-c}$ that we measure depends on V_c in such a way that $V_{\odot-c}$ is about 2 km s $^{-1}$ lower if $V_c = 240$ km s $^{-1}$. This dependence, however, only affects the above statement by a percent.

7. CONCLUSION AND OUTLOOK

In this paper we have investigated the two-dimensional line-of-sight velocity field in the MW mid-plane out to 5 kpc using APOGEE-RC stars. We have focused on two important questions: (a) the Sun's motion with respect to the circular velocity and (b) the residuals from an axisymmetric kinematic model. We characterized the latter using their power spectrum, finding that the power on scales in the range $0.2 \text{ kpc}^{-1} \leq k \leq 40 \text{ kpc}^{-1}$ is fully contained within $0.2 \text{ kpc}^{-1} \leq k \leq 0.9 \text{ kpc}^{-1}$, with the power on smaller scales consistent with measurement noise. The most likely perturber that creates power on these scales is the central bar.

We measured the Sun's motion with respect to the circular velocity using a new method based on minimizing the large-scale residuals in the peculiar velocity field. This approach unambiguously determines $V_{\odot-c}$ to be relatively large. In detail, we measure $V_{\odot-c} = 24 \pm 1$ (ran.) ± 2 (syst. [V_c]) ± 5 (syst. [large-scale]) km s $^{-1}$. Here, we have included systematic uncertainties due to (a) a 20 km s $^{-1}$ uncertainty in V_c and (b) the estimated

power on unobserved larger scales. This measurement agrees with the determination by B12, which employed an almost independent subsample of APOGEE data from the one used here and which used a different technique for inferring $V_{\odot-c}$.

In the future, much better measurements of the peculiar velocity field in the MW mid-plane will be possible with data from the *Gaia* satellite (Perryman et al. 2001) and from APOGEE-2. *Gaia* will allow both dimensions of the planar peculiar velocity field to be determined, rather than just the line-of-sight component as done here. APOGEE-2 will perform measurements at all Galactic longitudes and at much larger distances from the Sun in the dust-obscured regions of the disk, crucial for understanding the largest-scale modes affecting the disk's kinematics and for a complete interpretation of the optical *Gaia* data. Performing similar measurements with ongoing surveys of resolved kinematics in galaxies (e.g., CALIFA, Sánchez et al. 2012; SAMI, Croom et al. 2012; MANGA, Bundy et al. 2015) will be difficult because of the relatively low spectral resolution and typical signal-to-noise ratios of these surveys. However, MUSE (Bacon et al. 2010) could be used to create maps with high enough velocity resolution to determine the power spectrum on the largest scales in nearby galaxies, which would provide an interesting look into the drivers of galaxy evolution in different types of galaxies and environments. Connecting these measurements to that in the Milky Way will be crucial for determining the exact characteristics and origin of the power in the velocity field on large scales and their implications for the dynamical evolution of stellar populations in galactic disks.

J.B. gratefully acknowledges various insightful conversations with Scott Tremaine about the MW velocity field and how to best characterize it as well as detailed comments on this paper. It is also a pleasure to thank Simeon Bird for discussions of two- and one-dimensional power spectra, and Hans-Walter Rix, Annie Robin, Donald Schneider, Matthias Steinmetz, David Weinberg, and the

anonymous referee for helpful discussions and comments. We also thank Simone Callegari, Javiera Guedes, Piero Madau, and Lucio Mayer for sharing the ErisLE simulation with us. J.B. was supported by NASA through Hubble Fellowship grant HST-HF-51285.01 from the Space Telescope Science Institute, which is operated by the Association of Universities for Research in Astronomy, Incorporated, under NASA contract NAS5-26555. J.B. further acknowledges support from a John N. Bahcall Fellowship and the W.M. Keck Foundation. J.C.B. acknowledges the support of the Vanderbilt Office of the Provost through the Vanderbilt Initiative in Data-intensive Astrophysics (VIDA). S.R.M. was supported by NSF grants 1109718 and 1413269.

Funding for RAVE (www.rave-survey.org) has been provided by institutions of the RAVE participants and by their national funding agencies.

Funding for SDSS-III has been provided by the Alfred P. Sloan Foundation, the Participating Institutions, the National Science Foundation, and the U.S. Department of Energy Office of Science. The SDSS-III web site is <http://www.sdss3.org/>.

SDSS-III is managed by the Astrophysical Research Consortium for the Participating Institutions of the SDSS-III Collaboration including the University of Arizona, the Brazilian Participation Group, Brookhaven National Laboratory, Carnegie Mellon University, University of Florida, the French Participation Group, the German Participation Group, Harvard University, the Instituto de Astrofísica de Canarias, the Michigan State/Notre Dame/JINA Participation Group, Johns Hopkins University, Lawrence Berkeley National Laboratory, Max Planck Institute for Astrophysics, Max Planck Institute for Extraterrestrial Physics, New Mexico State University, New York University, Ohio State University, Pennsylvania State University, University of Portsmouth, Princeton University, the Spanish Participation Group, University of Tokyo, University of Utah, Vanderbilt University, University of Virginia, University of Washington, and Yale University.

REFERENCES

- Athanassoula, E. 2003, *MNRAS*, 341, 1179
 Bacon, R., Accardo, M., Adjali, L., et al. 2010, *Proc. SPIE*, 7735, 08
 Barbanis, B. & Woltjer, L. 1967, *ApJ*, 150, 461
 Bensby, T., Oey, M. S., Feltzing, S., & Gustafsson, B. 2007, *ApJ*, 655, 89
 Binney, J. & Lacey, C. 1988, *MNRAS*, 230, 597
 Binney, J., Gerhard, O. E., Stark, A. A., Bally, J., & Uchida, K. I. 1991, *MNRAS*, 252, 210
 Binney, J. J., Gerhard, O., & Spergel, D. N. 1997, *MNRAS*, 288, 365
 Binney, J. & Tremaine, S. 2008, *Galactic Dynamics: Second Edition* (Princeton, NJ: Princeton Univ. Press)
 Binney, J. 2010, *MNRAS*, 401, 2318
 Binney, J., Burnett, B., Kordopatis, G., et al. 2014, *MNRAS*, 437, 351
 Bird, J. C., Kazantzidis, S., Weinberg, D. H., et al. 2013, *ApJ*, 773, 43
 Bissantz, N. & Gerhard, O. 2002, *MNRAS*, 330, 591
 Blitz, L. & Spergel, D. N. 1991, *ApJ*, 379, 631
 Bournaud, F., Elmegreen, B. G., & Martig, M. 2009, *ApJ*, 707, 1
 Bovy, J. 2010, *ApJ*, 725, 1676
 Bovy, J. & Hogg, D. W. 2010, *ApJ*, 717, 617
 Bovy, J., Allende Prieto, C., Beers, T. C., et al. 2012, *ApJ*, 759, 131 (B12)
 Bovy, J. & Rix, H.-W. 2013, *ApJ*, 779, 115
 Bovy, J., Nidever, D. L., Rix, H.-W., et al. 2014, *ApJ*, 790, 127
 Bovy, J. 2015, *ApJS*, in press (arXiv:1412.3451)
 Bressan, A., Marigo, P., Girardi, L., et al. 2012, *MNRAS*, 427, 127
 Brook, C. B., Kawata, D., Gibson, B. K., & Freeman, K. C. 2004, *ApJ*, 612, 894
 Bundy, K., Bershady, M. A., Law, D. R., et al. 2015, *ApJ*, 798, 7
 Burton, W. B. 1971, *A&A*, 10, 76
 Carlberg, R. G. & Sellwood, J. A. 1985, *ApJ*, 292, 79
 Carlberg, R. G. 1987, *ApJ*, 322, 59
 Carlin, J. L., Majewski, S. R., Casetti-Dinescu, D. I., et al. 2012, *ApJ*, 744, 25
 Contopoulos, G. 1980, *A&A*, 81, 198
 Croom, S. M., Lawrence, J. S., Bland-Hawthorn, J., et al. 2012, *MNRAS*, 421, 872
 Debattista, V. P. & Sellwood, J. A. 2000, *ApJ*, 543, 704
 Debattista, V. P., Mayer, L., Carollo, C. M., et al. 2006, *ApJ*, 645, 209
 Dehnen, W. 1998, *AJ*, 115, 2384
 Dehnen, W. & Binney, J. J. 1998, *MNRAS*, 298, 387
 Dehnen, W. 1999, *AJ*, 118, 1201
 Dehnen, W. 2000, *AJ*, 119, 800

- De Simone, R., Wu, X., & Tremaine, S. 2004, MNRAS, 350, 627
- Dwek, E., Arendt, R. G., Hauser, M. G., et al. 1995, ApJ, 445, 716
- Eisenstein, D. J., Weinberg, D. H., Agol, E., et al. 2011, AJ, 142, 72
- ESA 1997, The *Hipparcos* and Tycho Catalogues (Noordwijk: ESA: ESA SP-1200)
- Famaey, B., Siebert, A., & Jorissen, A. 2008, A&A, 483, 453
- Faure, C., Siebert, A., & Famaey, B. 2014, MNRAS, 440, 2564
- Ghez, A. M., Salim, S., Weinberg, N. N., et al. 2008, ApJ, 689, 1044
- Gillessen, S., Eisenhauer, F., Trippe, S., Alexander, T., Genzel, R., Martins, F., Ott, T. 2009, ApJ, 692, 1075
- Guedes, J., Callegari, S., Madau, P., & Mayer, L. 2011, ApJ, 742, 76
- Guedes, J., Mayer, L., Carollo, M., & Madau, P. 2013, ApJ, 772, 36
- Gunn, J. E., Siegmund, W. A., Mannery, E. J. et al. 2006, AJ, 131, 2332
- Hänninen, J. & Flynn, C. 2002, MNRAS, 337, 731
- Hogg, D. W., Blanton, M. R., Roweis, S. T., & Johnston, K. V. 2005, ApJ, 629, 268
- Ida, S., Kokubo, E. & Makino, J. 1993, MNRAS, 263, 875
- Jenkins, A. & Binney, J. 1990, MNRAS, 245, 305
- Kordopatis, G., Gilmore, G., Steinmetz, M., et al. 2013, AJ, 146, 134
- Kuijken K. & Tremaine, S. 1994, ApJ, 421, 178
- Lacey, C. G. & Ostriker, J. P. 1985, ApJ, 299, 633
- Laney, C. D., Jonek, M. D., & Pietrzyński, G. 2012, MNRAS, 419, L1637
- Levine, E. S., Heiles, C., & Blitz, L. 2008, ApJ, 679, 1288
- Majewski, S. R., Zasowski, G., & Nidever, D. L. 2011, ApJ, 739, 25
- Metzger, M. R., Caldwell, J. A. R., & Schechter, P. L. 1998, AJ, 115, 635
- Minchev, I. & Famaey, B. 2010, ApJ, 722, 112
- Mühlbauer, G. & Dehnen, W. 2003, A&A, 401, 975
- Nordström, B., Mayor, M., Andersen, J., et al. 2004, A&A, 418, 989
- Perryman, M. A. C., de Boer, K. S., Gilmore, G., et al. 2001, A&A, 369, 339
- Press, W. H., Teukolsky, S. A., Vetterling, W. T., & Flannery, B. P., 2007, Numerical Recipes: The Art of Scientific Computing, 3rd Edition (Cambridge University Press)
- Quinn, P. J., Hernquist, L., & Fullagar, D. P. 1993, ApJ, 403, 74
- Reid, M. J. & Brunthaler, A. 2004, ApJ, 616, 872
- Rix, H.-W. & Zaritsky, D. 1995, ApJ, 447, 82
- Sánchez, S. F., Kennicutt, R. C., Gil de Paz, A., et al. 2012, A&A, 538, A8
- Schönrich, R., Binney, J. J., & Dehnen, W. 2010, MNRAS, 403, 1829
- Sellwood, J. A. & Binney, J.J. 2002, MNRAS, 336, 785
- Sellwood, J. A. 2010, MNRAS, 409, 145
- Siebert, A., Famaey, B., Minchev, I., et al. 2011, MNRAS, 412, 2026
- Sharma, S., Bland-Hawthorn, J., Binney, J., et al. 2014, ApJ, 793, 51
- Shuter, W. L. H. 1982, MNRAS, 199, 109
- Sobeck, J., Majewski, S., Hearty, F., et al. 2014, in American Astronomical Society Meeting Abstracts, 223, #440.06
- Spitzer, L., Jr. & Schwarzschild, M. 1951, ApJ, 114, 385
- Steinmetz, M., Zwitter, T., Siebert, A., et al. 2006, AJ, 132, 1645
- Stinson, G. S., Bovy, J., Rix, H.-W., et al. 2013, MNRAS, 436, 625
- Toth, G. & Ostriker, J. P. 1992, ApJ, 389, 5
- Velazquez, H. & White, S. D. M. 1999, MNRAS, 304, 254
- Visser, H. C. D. 1980, A&A, 88, 149
- Weinberg, M. D. 1985, MNRAS, 213, 451
- Weiner, B. J. & Sellwood, J. A. 1999, ApJ, 524, 112
- Wielen, R. 1977, A&A, 60, 263
- Williams, M. E. K., Steinmetz, M., Binney, J., et al. 2013, MNRAS, 436, 101
- Wilson, J. C., Hearty, F., Skrutskie, M. F., et al. 2010, Proc. SPIE, 7735, 46
- Yuan, C. 1969, ApJ, 158, 871
- Zasowski, G., Johnson, J. A., Frinchaboy, P. M., et al. 2013, AJ, 146, 81
- Zhao, H. & Mao, S. 1996, MNRAS, 283, 1197